A retinotopic reference frame for space throughout human visual cortex

Martin Szinte[1,2,*], Gilles de Hollander[2,3*], Marco Aqil[2,4,5*],
Inês Veríssimo[2,5], Serge Dumoulin[2,4,5,6], Tomas Knapen[2,4,5]
1. Institut de Neurosciences de la Timone, CNRS & Aix-Marseille Université, UMR 7289, Marseille, France.
2. Spinoza Centre for Neuroimaging, Royal Dutch Academy of Sciences, Amsterdam, Netherlands.
3. Zurich Center for Neuroeconomics, Department of Economics, University of Zurich, Switzerland
4. Computational Cognitive Neuroscience and Neuroimaging, Netherlands Institute for Neuroscience, Amsterdam, Netherlands
5. Department of Cognitive Psychology, Vrije Universiteit Amsterdam, Amsterdam, Netherlands.
6. Department of Experimental Psychology, Utrecht Universiteit, Utrecht, Netherlands.
* First-author equal contribution

Summary

We perceive a stable visual world across eye movements, despite the drastic retinal transients these movements produce. To explain vision's spatial stability, it has been suggested that the brain encodes the location of attended visual stimuli in an external, or spatiotopic, reference frame. However, spatiotopy is seemingly at odds with the fundamental retinotopic organization of visual inputs. Here, we probe the spatial reference frame of vision using ultra-high-field (7T) fMRI and single-voxel population receptive field mapping, while independently manipulating both gaze direction and spatial attention. To manipulate spatial attention, participants performed an equally demanding visual task on either a bar stimulus that traversed the visual field, or a small foveated stimulus. To dissociate retinal stimulus position from its real-world position the entire stimulus array was placed at one of three distinct horizontal screen positions in each run. We found that population receptive fields in all cortical visual field maps shift with the gaze, irrespective of how spatial attention is deployed. This pattern of results is consistent with a fully retinotopic reference frame for visual-spatial processing. Reasoning that a spatiotopic reference frame could conceivably be computed at the level of entire visual areas rather than at the level of individual voxels, we also used Bayesian decoding of stimulus location from the BOLD response patterns in visual areas. We found that decoded stimulus locations also adhere to the retinotopic frame of reference, by shifting with gaze position. Again, this result holds for all visual areas and irrespective of the deployment of spatial attention. We conclude that visual locations are encoded in a retinotopic reference frame throughout the visual hierarchy.

Keywords

Retinotopy, population receptive field, Bayesian decoding, ultra-high-field fMRI

Introduction

Eye movements rapidly alter the projection of visual objects on the retina. Nevertheless, our subjective visual perception is stable and invariant to these eye movements. This "*space constancy*" phenomenon presents researchers with a conundrum: how do our brains build a stable impression of the world based on such fleeting, jumbled sensory inputs? One major step to understanding space constancy would be to answer the question of how the information of visual objects' location is represented by the visual system.

Visual location is first encoded by the retina[1], whose topography is maintained as spatial information is transmitted to subsequent processing stage[2,3]. Foundationally, visual locations are encoded in a common "retinotopic" reference frame[4,5], keeping the retinal photoreceptors organization. Neural responses in this retinotopic reference frame are modulated by gaze direction[6,7]. This combination of action-related and visual sources of information is thought to allow the brain to localize objects in the outside world[8–10]. But the precise mechanisms underpinning world-centered localization, including the role of spatial attention, remain a matter of debate[11–14]. Specifically, an open fundamental question is whether gaze modulation of visual information leads to the encoding of locations of visual stimuli in a spatiotopic frame of reference.

Here, we leveraged population receptive field (pRF) estimation[15] and ultra-high-field (7T) whole brain fMRI to probe the spatial reference frame of vision at the level of local neural populations sampled by individual voxels. We determined voxels' pRF position while participants directed their gaze to three distinct locations, allowing us to test whether pRFs are pinioned to the outside world (the *spatiotopic* hypothesis), or fixed to the retina (the *retinotopic* hypothesis). To study the role of spatial attention, participants performed an equally demanding orientation-discrimination task either at fixation or on a moving visual-mapping stimulus. We found that throughout the cortical visual hierarchy, pRFs systematically shift with gaze, as being fixed to the retina, irrespective of where spatial attention is deployed. Next, to probe the visual reference frame at the level of entire visual field maps, we adapted a Bayesian decoding method[16–18], to infer the spatial properties of our visual stimuli from the pattern of voxel responses in entire visual areas. In line with our single-voxel results, we found that decoded stimulus locations are fixed to the retina, again favoring the retinotopic hypothesis. Altogether our results suggest that location is represented throughout the visual hierarchy by populations of receptive fields operating in a retinotopic reference frame.

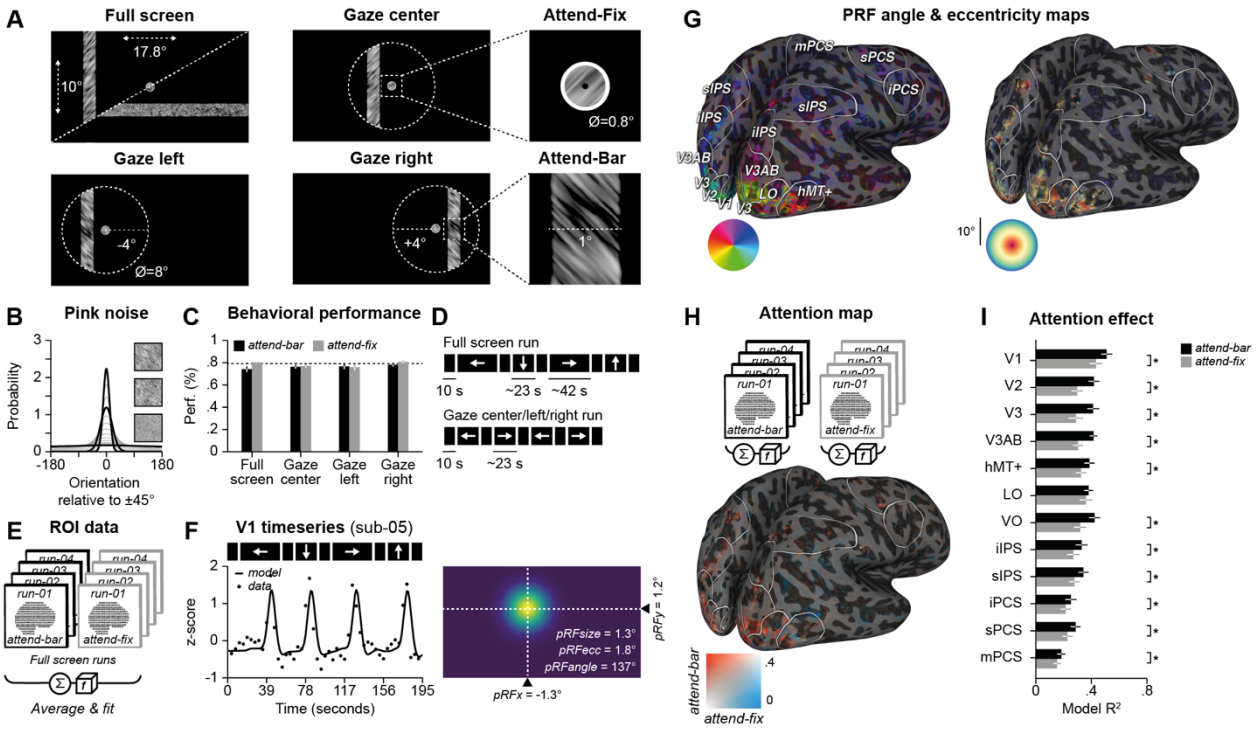

Figure 1. Methods, pRF modeling and attention effect. A. Participants fixated a bull's-eye in either *full screen* (top left panel), *gaze center* (top center), *gaze left* (bottom left) and *gaze right* runs (center left). They reported the orientation of pink noise patterns (+45° or –45°) presented either within the bar (*attend-bar*) or within the fixation bull's-eye (*attend-fix*). **B.** We titrated the difficulty of the orientation discrimination task by varying the dispersion coefficient of the orientation filter applied to the pink noise pattern. The figure presents probability distributions of orientations contained within the pink noise patterns as a function of the dispersion coefficient. Right insets, showcase three levels of difficulty from non-oriented random noise (bottom) to the most oriented pattern used (top). **C.** Group performance (n = 8, two sessions each) obtained in the *attend-bar* (black) and *attend-fix* (gray) conditions. Error bars show ±SEM and the dashed line shows the staircase convergence level (~79% correct). **D.** In the *full screen* and *gaze center/left/right* conditions, a bar moved in different directions (black rectangles with arrows) interleaved with periods in which only the fixation bull's-eye was shown (empty black rectangles). **E.** To determine regions of interest (ROIs), we averaged *full screen* runs and fit a linear pRF model. **F.** Example V1 timeseries and its best explained pRF model and parameters. **G.** Single participant (*sub-005*) pRF angle and eccentricity maps projected on his inflated brain. Lines on the cortex delineate ROIs. Participants brains visualizations are available online (invibe.nohost.me/gazeprf/). **H.** Map of the effect of spatial attention obtained by comparing the explained variance of *attend-bar* and *attend-fix* conditions separately. Reddish colors of the inflated cortex illustrate the effect of spatial attention. **I.** Model explained variance (R^2) observed for the best-fitting voxels of each ROI in the *attend-bar* (black) and *attend-fix* (gray) conditions. Error bars show ±SEM, asterisks show significant difference between conditions (two-sided $p < 0.05$).

Results

PRF modeling and attention effect

Participants were instructed to continuously fixate a bull's-eye on a black background while horizontal and vertical bars swiped across the full extent of the screen (Fig. 1A, *full screen*). They reported the orientation of noise patterns presented either within the moving bar (*attend-bar* condition) or within the fixation bull's-eye (*attend-fix* condition). We titrated the difficulty of the task with a staircase procedure which adjusted the orientation dispersion coefficient of pink noise patterns inside the presented stimuli (Fig. 1B). Participants maintained the expected staircase performance level (Fig. 1C, *full screen, attend-bar*: 74.06% ± 2.50; *full screen, attend-fix*: 80.26% ± 0.40), confirming their ability to attend to the noise patterns presented in the periphery or at fixation with equal performance. Apart from the attention task, the stimulus presentation sequence of *full screen* followed an identical sequence (Fig. 1D, top), allowing us to average signal timeseries across the attention tasks (Fig. 1E) into a single, high-SNR *fiducial* timeseries.

From each voxel's fiducial timeseries, we quantified the screen locations at which a stimulus evokes a visual response by estimating its population receptive field properties. Specifically, we fit a linear, isotropic Gaussian pRF model to find optimal location (*pRFx* and *pRFy*) and size (*pRFsize*) parameters that quantify the spatial tuning of the neural population within each voxel. Figure 1F shows an example of a V1 voxel timeseries and its best-fitting pRF model. From the position parameters, we derived pRF eccentricity and pRF angle maps that can be projected onto individual participants' cortical surfaces (Fig. 1G) to delineate visual field maps as regions of interests (see Methods). We next repeated this analysis using timeseries of *attend-bar* and *attend-fix* runs averaged separately (Fig. 1H, top), using the fiducial outcomes as starting parameters. Figure 1H show an inflated cortex of a participant displaying the change in explained variance (R^2) resulting from manipulating spatial attention. Using the 250 best-fitting voxels per ROI, we found a significant improvement of the explained variance when comparing the *attend-bar* to the *attend-fix* conditions for all ROIs (*attend-bar*: 0.51 > R^2 > 0.18 vs. *attend-fix:* 0.43 > R^2 > 0.15, 0.0117 > *ps* > 0.0001, two-sided *p* values) except area LO (*attend-fix*: R^2: 0.38 ± 0.03 vs. *attend-bar* R^2: 0.36 ± 0.04, two-sided *p* = 0.24). This pattern of result was similar when including all voxels contained within the ROIs. Taken together, behavioral and functional imaging results illustrate classical effects of visual spatial attention: an improvement of orientation discrimination abilities[19,20] correlated with an improvement of the corresponding fMRI BOLD signal-to-noise-ratio[21,22].

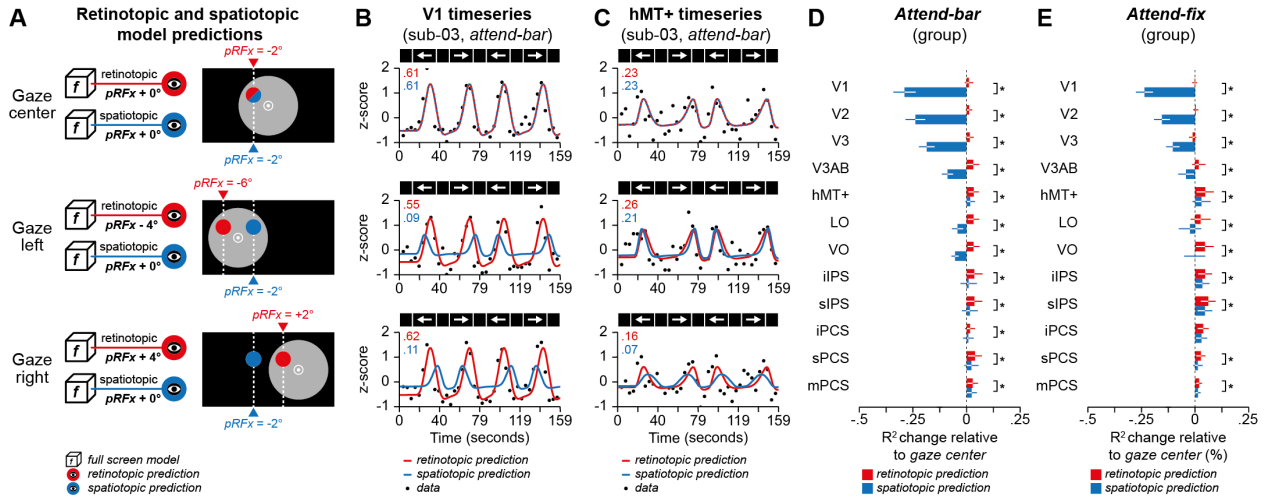

Figure 2. Out-of-sample retinotopic and spatiotopic predictions. A. Retinotopic predictions are obtained by adding the change in gaze direction to the *full screen pRFx* parameters (e.g., $pRFx_{gaze\ left} = pRFx_{full\ screen} - 4°$). The spatiotopic hypothesis dictates that the *pRFx* should stay identical irrespective of the gaze direction (i.e., $pRFx_{gaze\ left} = pRFx_{gaze\ right} = pRFx_{gaze\ center} = pRFx_{full\ screen}$). **B-C**. Example retinotopic (red) and spatiotopic (blue) timeseries predictions for V1 (B) and hMT+ voxels (C) in the *gaze center* (top row), *gaze left* (middle row) and *gaze right attend-bar* runs of one participant (sub-003). Leftmost inset values show corresponding model R^2. **D-E.** Retinotopic (red) and spatiotopic predictions (blue) change in explained variance between *gaze left/right* and *gaze center* conditions across ROIs. Note that only spatiotopic prediction of V1, V2 and V3 voxels display a significant change as compared to zero in both attention conditions (V1/V2/V3: 0.0156 > *ps* > 0.0001; two-sided *p* values), as well as V3AB (two-sided *p* = 0.0156) and VO in the attend-bar condition (two-sided *p* = 0.0078). Error bars show ±SEM, asterisks show significant difference between retinotopic and spatiotopic predictions (two-sided $p < 0.05$).

Out-of-sample predictions show retinotopic encoding of visual space

We next aimed to use the pRF estimates from the *full-screen* condition to probe the reference frame of spatial vision. Across runs, participants were instructed to fixate their gaze either at the screen center (Fig. 1A, *gaze center*), to the left (Fig. 1A, *gaze left*) or to the right of it (Fig. 1A, *gaze right*). The entire mapping stimulus sequence was centered on these fixation locations, and was restricted to vertical bars moving rightward or leftwards, vignetted by a circular aperture (Fig. 1A and Fig. 1D). Again, participants reported

the orientation of noise patterns presented within the bar (*attend-bar*) or within the fixation bull's-eye (*attend-fix*). They reached the staircase expected performance level in the *gaze center* (Fig. 1C, *attend-bar*: 76.27% ± 1.67; *attend-fix*: 76.95% ± 1.48), the *gaze left* (Fig. 1C, *attend-bar*: 76.59% ± 2.30; *attend-fix*: 75.88% ± 2.49) and *gaze right* conditions (Fig. 1C, *attend-bar*: 78.09% ± 1.66; *attend-fix*: 80.61% ± 1.25). Using the *full screen* experiment's pRF parameters, we calculated predicted timeseries for the *gaze center*, *gaze left* and *gaze right* conditions in the retinotopic and spatiotopic reference frame. Specifically, to obtain retinotopic predictions we added the gaze direction change to the *pRFx* parameter (x-coordinate of the pRF) obtained in the corresponding *full screen* conditions (Fig. 2B, *retinotopic prediction*). The spatiotopic hypothesis supposed that the *pRFx* do not vary as a function of the gaze directions (Fig. 2A, *spatiotopic prediction*). We thus kept the *pRFx* parameter as observed in the corresponding *full screen* conditions. Figure 2B-C illustrate the predicted and measured timeseries of V1 and hMT+ voxels. We highlighted these regions to relate them to former studies reporting spatiotopic effects[11,12].

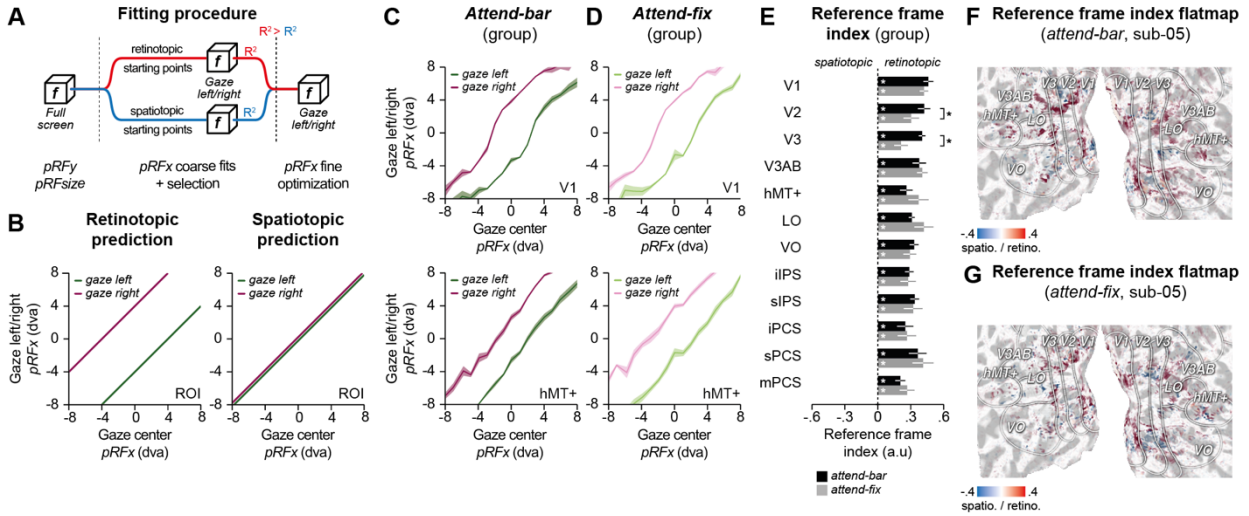

Figure 3. Fitting retinotopic and spatiotopic pRF models. A. Fitting procedure. We used a coarse-to-fine optimization fitting procedure in which we kept the *pRFy* and *pRFsize* parameters from the corresponding *full screen* runs. In order to avoid bias between the spatiotopic and retinotopic model, we first used two different sets of parameter starting points. These starting points were based on either the retinotopic (red) or the spatiotopic (blue) hypotheses. For a next optimization stage, we selected the parameters producing the highest fit quality. **B.** Retinotopic and spatiotopic predictions. The gaze center *pRFx* as a function of the *gaze left/right pRFx* will either shift (left panel, retinotopic prediction) or remain at the same position (right panel, spatiotopic prediction) when comparing the *gaze center* with the *gaze left* (green) or *gaze right* conditions (purple). **C-D.** Each panel shows the group average of 16 equal bins of the *pRFx* obtained in the *gaze center* runs as a function of the corresponding group averaged bins of the *pRFx* obtained in the *gaze left* (purple) and *gaze right* runs (green) for the *attend-bar* (C, dark colors) and *attend-fix* conditions (D, light colors). Error areas show ±SEM. **E.** Group average reference frame index (RFI) observed in the *attend-bar* (black) and *attend-fix* conditions (gray) for the best-fitting voxels of each ROI. Error bars show ±SEM, white asterisks show significant RFI as compared to a null effect (two-sided $p < 0.05$). Black asterisks indicate a significant difference between the *attend-bar* and *attend-fix* conditions (two-sided $p < 0.05$). **F-G.** Reference frame index maps obtained by projecting the RFI obtained in the *attend-bar* (F) and *attend-fix* conditions (G) on inflated cortex using a unimodal color scale (blue: spatiotopic vs. red: retinotopic) for a participant (sub-05, same as in Fig. 1).

Importantly, the gaze center condition can serve as a baseline: both the spatiotopic and retinotopic predictions necessarily produce identical pRFx parameters. We computed the change in the pRF model explained variance (R^2) between the gaze left and gaze right runs as compared to the gaze center runs. We found, again using the best 250 voxels across ROIs, significantly lower explained variance for the spatiotopic relative to the retinotopic prediction in both the attend-bar (Fig. 2D, spatiotopic prediction:

+2.36% > R^2 change > -28.91% vs. retinotopic prediction: +3.96 > R^2 change > +1.09%, 0.0195 > ps > 0.0001, two-sided p values) and attend-fix conditions (Fig. 2E, spatiotopic prediction: +4.61% > R^2 change > -23.59% vs. retinotopic prediction: +6.14 > R^2 change > -1.12%, 0.0352 > ps > 0.0001, two-sided p values). Similar effects were found when including all voxels contained within the ROIs.

Fitting pRFs positions shows retinotopic encoding of visual space

The results presented above suggest that the visual system encodes location in a retinotopic reference frame. However, our first analysis did not allow the *pRFx* parameter to vary in between the retinotopic and spatiotopic predictions, which could have provided evidence for spatiotopic representations of visual space. Thus, we fit the *horizontal pRF position* parameter in the gaze conditions while keeping the other pRF parameters constant (*pRFy* and *pRFsize*). To avoid any bias due to the starting points of the fitting procedure, we initiated parameters from distinct *horizontal pRF position* values referenced against either the gaze position (Fig. 3A, retinotopic starting points) or the screen center (Fig 3A, spatiotopic starting points). In a subsequent stage, we optimized the *horizontal pRF position* parameter starting from the highest explained variance model (R^2) of the first stage. We formulated two distinct predictions based on our two competing hypotheses. We used the *gaze center* condition as a reference for both hypotheses, since they produce identical predictions. In the retinotopic reference frame hypothesis, *horizontal pRF position* in the *gaze left* and *gaze right* conditions shifts based on gaze direction (Fig. 3B, retinotopic prediction). Conversely, in the spatiotopic reference frame hypothesis, *horizontal pRF position* shouldn't differ from that observed when participants look straight ahead (Fig. 3B, spatiotopic prediction). Figure 3C and Figure 3D show these comparisons across participants for best-fitting voxels of V1 and hMT+ using data modeled from the *attend-bar* and *attend-fix* runs respectively. In accordance with previous studies[11–13], results suggest that V1 uses a retinotopic frame of reference irrespective of where participant deploy their spatial attention (Figure 3C-D, top). Our results suggest that hMT+ also uses a retinotopic framework, regardless of spatial attention's focus (Figure 3C-D, bottom).

To evaluate quantitatively which reference frame best explains our results at the level of individual voxels across all ROIs, we computed a reference frame index (RFI, see Methods), computed as in previous studies[11,13]. Briefly, it quantifies the difference in explained variance between the two model classes on a scale between -1 and 1, where pure spatiotopy corresponds to -1, pure retinotopy to +1, and noise results in an RFI value of 0. Figure 3E shows RFI obtained with the best-fitting voxels of each ROI for the *attend-bar* and *attend-fix* conditions. Across participants, RFI were significantly positive for all ROIs in the *attend-bar* (0.46 > RFI > 0.20, 0.0312 > *ps* > 0.0001, two-sided *p* values) and *attend-fix* conditions (0.42 > RFI > 0.21, 0.0312 > *ps* > 0.0001, two-sided *p* values). Moreover, RFI values did not differ between conditions in all ROIs (*attend-bar*: 0.93 > *ps* > 0.38, two-sided *p* values), apart from V2 (*attend-bar* RFI: 0.42 ±0.06 vs. *attend-fix* RFI: 0.30 ± 0.08, two-sided $p < 0.01$) and V3 (*attend-bar* RFI: 0.40 ±0.03 vs. *attend-fix* RFI: 0.21 ± 0.07, two-sided $p < 0.01$). Similar statistics were observed when including all voxels. This analysis suggests that at the level of individual voxels, visual location is encoded in a retinotopic reference frame irrespective of the deployment of attention. Figure 3F and 3G illustrate these effects by projecting the RFI onto the cortical surface of a single participant when he attended stimuli presented within the bar (Fig. 3F) or within the fixation bull's-eye (Fig. 3G).

Bayesian decoding of visual field positions shows retinotopic encoding of visual space

Even if local populations of neurons sampled by single voxels do not show evidence of spatiotopic location coding, more dispersed effects across the entire visual field map might conceivably provide the means for the brain to represent world-centered coordinates. Such a mechanism might only be evident when inferring the locations of visual stimuli from the pattern of BOLD responses across an entire visual region, while taking into account the covariance structure between voxels. Thus, we next aimed at decoding, for

each individual ROI, the position of the moving bar for different gaze conditions. We adapted a Bayesian decoding method developed for estimating, from a pattern of BOLD responses, a full posterior distribution along a single stimulus dimension, namely visual orientation[16], to the multiple stimulus dimensions of visual space. Our novel method decodes bar spatial locations on a TR-by-TR basis (see *Methods*), based on pRF estimates and residual covariance structure from the *full screen* runs (Fig. 4A). Contrary to techniques which decode a single stimulus value most consistent with the observed data, Bayesian decoding also produces uncertainty estimates for the decoded features. This decoded uncertainty has been shown to relate to sensory uncertainty and decision confidence[16,23]. Our method determines, for every TR, the full posterior probability along spatial bar location parameters based on the per-TR BOLD pattern in the *gaze center*, *gaze left* or *gaze right* conditions (Fig. 4B). Because this posterior distribution lives in visual space it can be compared to the ground truth of what was actually shown on the screen to participants.

Crucially, we can define distinct spatiotopic and retinotopic predictions for the reference frame in which the decoded bar position is hypothesized to reside. As our decoder was trained on the *full screen* dataset in which participants fixated straight ahead, the spatiotopic hypothesis predicts that our decoder will sense the change of gaze as a shift of the bar position in the opposite direction. Conversely, the retinotopic hypothesis predicts that the decoded position will be centered on the coordinates of the *full screen* stimulus, irrespective of gaze direction. Figure 4C shows the decoded position of the bar (i.e., the peak of the bar position distribution) as observed when considering V1 voxels from a single run of the *gaze center*, the *gaze left* and the *gaze right* conditions. Figure 4D-E shows for a participant the same effect averaged across runs and bar passes, for V1 (Fig. 4D) and hMT+ voxels respectively (Fig. 4E). To quantify decoding performance, we computed the correlation between the decoded position and the retinotopic ground truth of the moving bar (Fig. 4F). Correlations in the *attend-bar* condition were significantly positive for all ROIs ($0.77 > r > 0.13$, $0.0391 > ps > 0.0001$, two-sided p values) with the strongest correlations for low-level visual areas (e.g., V1, $r = 0.73 \pm 0.04$, $p < 0.01$; hMT+, $r = 0.70 \pm 0.05$, $p < 0.0001$, two-sided p values). Correlations were significantly positive in the *attend-fix* condition across all ROIs ($0.67 > r > 0.17$, $0.0078 > ps > 0.0001$, two-sided p values), except for sIPS ($r = 0.02 \pm 0.03$, two-sided $p = 0.49$) and iPCS ($r = 0.07 \pm 0.05$, two-sided $p = 0.21$). Furthermore, when participants directed spatial attention to the moving barn, correlations were significantly increased when compared to *attend-fix* condition in all ROIs (*attend-bar* vs. *attend-fix*, $0.0391 > ps > 0.0001$, two-sided p values), apart from V3 (two-sided $p = 0.09$), hMT+ (two-sided $p = 0.06$) and iPCS (two-sided $p = 0.21$).

To answer our central question concerning visual reference frames, we again computed a RFI based on these decoding results (see Methods) for each participant and ROI (Fig. 4E, see *Methods*). Across participants, RFIs were significantly positive across all ROIs, indicating a predominant retinotopic reference frame in both the *attend-bar* ($0.71 > RFI > 0.51$, $0.0078 > ps > 0.0001$, two-sided p values) and *attend-fix* conditions ($0.64 > RFI > 0.47$, $0.0078 > ps > 0.0001$, two-sided p values). Deployment of attention to the bar stimulus increased the RFI for V1, V3AB, iIPS, sPCS and mPCS ($0.0391 > ps > 0.0078$, two-sided p values), indicating that increased decoding fidelity increases the strength of retinotopic representations in both low and high levels of the visual hierarchy. Lastly, we inspected whether the decoder's uncertainty perhaps provides residual indications for any role of spatiotopic spatial coding of visual locations. Specifically, the mismatch between train and test set due to differences in gaze location should increase uncertainty for gaze left and gaze right conditions relative to the gaze center condition. We quantified the uncertainty of the decoder by calculating the dispersion of the posterior along the horizontal position dimension. In the intermediate layers of the visual system, specifically in areas like V3AB, hMT+, LO, VO, and iIPS, we observed distinct outcomes of spatial attention. Specifically, when attention is directed towards the bar stimulus, there is a noticeable reduction in decoder uncertainty, aligning with the previously explained impacts on decoding fidelity (Supp. Fig. 1A). The impact of decoder uncertainty on attention was significantly more pronounced than any influence of gaze direction (Supp Fig. 1B).

Altogether these effects indicate that visual areas represent visual locations using a retinotopic reference frame irrespective of the deployment of attention, also when taking into account the region-level covariance structure of BOLD responses.

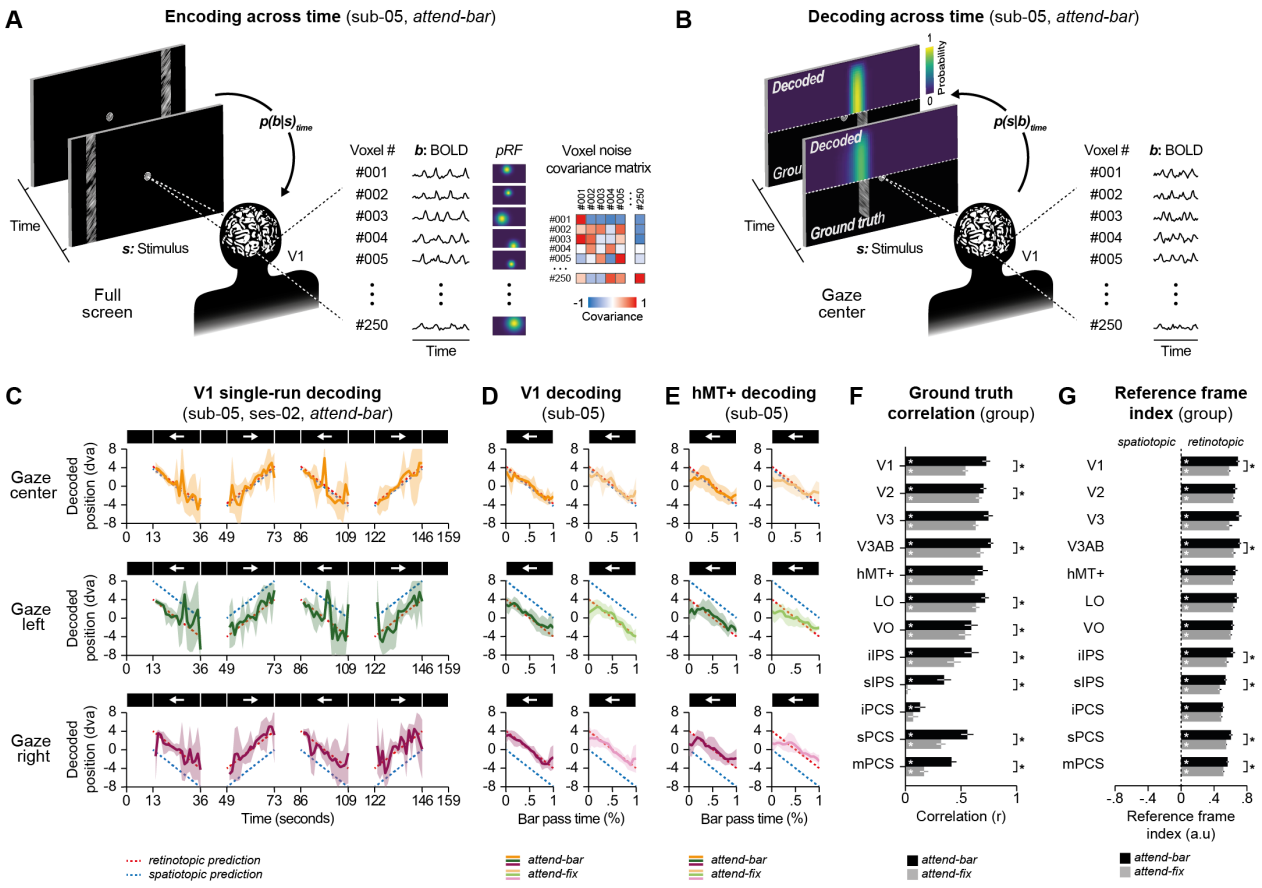

Figure 4. Bayesian decoding. A. Our encoding procedure consists of determining a likelihood $p(b|s)_{time}$ defined as the probability of observing fMRI BOLD signal (*b*) as a function of the stimulus (*s*) presented in the *full screen* condition. For this analysis we use the spatial tuning and noise correlations of the 250 best-fitting voxels per ROI. **B.** The decoding procedure illustrated here computes the posterior probability over time $p(s|b)_{time}$ using independent recorded BOLD signals for example from the *gaze center* condition. This procedure results in a direct comparison of decoded and actual bar position over time (see comparison of posterior distribution sample and ground truth). **C.** Decoded bar position as function of the time in the gaze center (top, orange), the gaze left (middle, green) and the gaze right (bottom, purple) conditions. Graphs present decoding from individual runs (from the second session) using V1 voxels activity (*attend-bar* condition) of a participant (sub-05). Predictions are illustrated as red and blue dashed lines for the retinotopic and spatiotopic predictions, respectively. Error areas show the posterior distribution STD. **D-E.** Average decoded bar position across bar passes and sessions for best-fitting voxels of V1 (D) and hMT+ (E) respectively, for *gaze center* (top), *gaze left* (middle) and *gaze right* conditions(bottom), in the *attend-bar* (left panels, dark colors) and *attend-fix* conditions (right panels, light colors). Error areas show ±SEM. **F.** Group averaged correlation between the decoded bar position and the ground truth. Conventions are as in Figure 3E. **G.** Group average reference frame index observed in the *attend-bar* (black) and *attend-fix* conditions (gray) for the best-fitting voxels of each ROI. Conventions are as in Figure 3E.

Discussion

We determined the spatial reference frame of visual processing across the human visual hierarchy using a principled computational modeling approach. We estimated population receptive field parameters while participants directed their gaze to distinct points in outside-world space. This allowed us to directly juxtapose two competing hypotheses: that of retinotopic spatial coding moving with participants' gaze, and that of spatiotopic spatial coding fixed to the outside world or at least to the participant's head.

Confronting a conundrum of contradictory findings in the literature, we factorially manipulated both gaze direction and the deployment of spatial attention. In brief, we find that all regions showing responses tuned to visual spatial location, as gauged using the pRF model, are retinotopically organized. Moreover, our results indicate that the deployment of spatial attention has no bearing on the reference frame of visual location processing. We conclude that the human brain fundamentally encodes visual locations in a retinotopic reference frame throughout the visual hierarchy. Our findings restrict solutions to the space constancy problem, and increase the prominence of those centered on dynamic interactions between action and perception, such as trans-saccadic remapping driven by re-afferent motor signals.

In the present study, we sought to leverage the precision afforded by the combination of ultra-high-field fMRI's increased SNR and the quantitative pRF model of visual location tuning. This allowed us to determine the reference frame of visual responses at the local neural population level, in single voxels. We ensured that for all quantifications, differences in signal quality or pRF size would not bias our outcomes toward the retinotopic or spatiotopic reference frame, following the logic outlined by Gardner and colleagues[13]. We also took into account the fact that V1 neuron receptive fields and pRFs have a nonlinear normalization field penumbra extending up to a factor of eight beyond their classical linear extent[24]. This means that visual information impinging on peripheral retinal areas, such as the visual transients produced by eye movements, evoke measurable signal fluctuations in even the most central portions of our retinotopic maps. Indeed, only experiments in full darkness will suffice to fully rule out the misinterpretation of such visual signals originating from the periphery. Importantly, by employing static gaze positions throughout our experimental runs and decreasing the strength of peripheral visual stimulation, we explicitly prevent such spurious signals from producing false spatiotopic patterns in our data[7]. We conceptualized experiments and analyses to be able to unequivocally adjudicate between retinotopic and spatiotopic reference frames. A crucial step here was to explicitly formulate and directly compare quantitative predictions for both hypotheses, at the level of single-voxel time series and across populations of voxels within ROIs. Across subsequent analyses these direct comparisons between data and hypotheses' predictions consistently favored the retinotopic reference frame hypothesis as the fundamental spatial encoding scheme of visual cortex.

As for the role of attention, our results align with previous studies indicating that spatial attention enhances the fidelity of spatial representations[21,22]. Spatial attention is known to modulate pRF position in accordance with the predictions of gain-field models[25,26]. Our results indicate that enhanced signal fidelity afforded by spatial attention renders visual cortex more, not less (Figs 3E, 4F-G), retinotopically organized[11]. We conclude that the differential deployment of spatial attention does not result in changes in the retinotopic spatial reference frame of visual cortex.

Every day, we experience a stable visual world across our eye movements: an experience far removed from the flutter of images projected onto our retinae. Our results reframe and highlight the fundamental question of visual stability across gaze changes, shifting the focus to mechanisms that achieve this stability with a robustly retinotopic visual cortex. Different solutions to the space constancy problem have been proposed[27,28], we here review these solutions through the lens of our results. A first category of solutions to the space constancy problem relies on the use of proprioceptive information of the eye position in the skull. An influential computational model[29] supported by numerous findings in both low-level[30,31] and high-level visual areas[32,33] proposed that proprioceptive signal of gaze direction could be used to recover stimuli position across eye movements. These findings suggest that the gain of retinotopically organized neurons is modulated by a field which encodes the position of the animal's eye. It is known from electrophysiological studies that although neighboring neurons encode similar locations in retinotopic visual space, they experience wildly varying gain-field effects[31], reflecting a salt-and-pepper organization. We did not find an influence of gaze position at the level of individual voxels nor at the level of visual areas, which is possibly in line with this organization at the single neuron level. Other than the potential absence of structured gain field maps, other reasons, however, might have prevented us to find them. First, visual

display size used in fMRI studies only allows gaze direction changes smaller than what used in electrophysiology, although the magnitude of our gaze shifts is in the range of most saccades made during naturalistic viewing. Second, gain fields from animal studies involved modulation of neuronal activations while our results rely on fMRI BOLD signals, which only is an indirect proxy of neurons firing rates[34,35]. Third, the timescales at which these eye position gain fields impact spatial processing may be faster than those of our experimental runs. Thus, our results do not rule out gain field mediated solutions to space constancy. Rather, our results support these accounts, while emphasizing the importance of the retinotopic reference frame in their application[36].

A second category of solution involves the use of an efference copy[37] to correct the consequence of gaze direction changes either before or during an eye movement[38,39]. These corrections have been proposed to be performed on retinotopically organized visual maps with the process being orchestrated by visual attention[40,41]. Remapping was observed at both the single neuron measures in distinct visual maps[42], fMRI studies[43–45] and human behavior[46,47]. Our results are compatible with this proposal but do not test it. Indeed, it is important to note that in order to model voxel activity we asked participants to maintain steady gaze throughout each acquisition. They change gaze directions only between runs, and not across trials – an explicit design choice to avoid any peripheral visual stimulation arising from the eye movements. Nevertheless, as participants laid still with the head and body fixed, our experiments left as much space as possible for putative fundamental spatiotopic processes to occur (see also[14]). Our results thus rule out space constancy solutions relying on an early encoding of space within craniotopic or spatiotopic maps[11,12].

As we move up the visual hierarchy, responses become more spatially invariant. This invariance abstracts neural responses away from their exact retinal origins, and reduces their adherence to the retinotopic reference frame while allowing them to be influenced by factors such as attentional gain fields[25,26,48]. It is also clear from a host of canonical findings in the medial temporal lobe that the brain does indeed encode the location of the agent in world-centered space. Clearly, a host of different information sources such as self-motion[49–51], pictorial cues[52], and navigational affordances[53–55] play a role in generating world-centered representations in our everyday interactions with the world. We argue that this process must feature the continuous integration of low-level sensory and high-level world-centered information. Interestingly, hippocampus was shown to encode locations in visual space in both humans and rodents[56–58], indicating that world-centered and sensory-based spatial reference frames can coexist at higher levels of processing. These findings demonstrate that V1-hippocampus interaction highlight the intimate links between different sensory and world-centric reference frames. It is clear that oculomotor behavior plays a foundational role in drawing these links[59].

Conclusion

Modeling ultra-high-field human cortical activity, we probed the reference frame of spatial vision. We found, both the level of individual neural population and that of visual areas, that vision is organized retinotopically, irrespective of where we look or attend. These results point to solutions to the space constancy problem that use active correction mechanism by means of predictive or proprioceptive signals.

Methods

Ethics statement

This experiment was approved by the Ethics Committee of Vrije Universiteit Amsterdam and conducted in accordance with the Declaration of Helsinki. All participants gave written informed consent.

Participants

Eight students and staff members of the Spinoza Centre for Neuroimaging participated in the experiment (ages 21-40, 1 female, 4 authors). All except two authors were naïve to the purpose of the study and all

had normal or corrected-to-normal vision.

MRI data acquisition

Four T1-weighted (1.0 mm isotropic resolution) and one T2-weighted (1.0 mm isotropic resolution) structural scans were acquired for each participant at The Spinoza Centre for Neuroimaging on a Philips Achieva 3T scanner (Philips Medical Systems, Best, Netherlands) and a 32 channel receive-coil array with a single channel transmit coil. Functional data were collected at the same center on a Philips Achieva 7T scanner (Philips Medical Systems, Best, Netherlands) with a 32 channel receive-coil array with 8-channel transmit coil (Nova Medical, Wilmington, MA). Functional data were collected using a 3D-EPI sequence at a resolution of 1.8 mm isotropic with a 1.3 s volume acquisition time, 44 ms TR, 17 ms TE, consisting of 98 slices of 112 by 112 voxels covering the entire brain. SENSE acceleration was applied in both the Anterior-Posterior (2.61-fold) and Right-Left (3.27-fold) directions. To estimate and correct susceptibility-induced distortions, we acquired an identical EPI image with an opposite phase encoding direction, after each functional scan. Transmit field homogeneity was improved by adjusting the 8-channel transmit output based on a B1+ field population template (i.e., "universal pulse"[60]).

Stimuli and tasks

The experiment consisted of 3 experimental sessions on different days. Participants started with two fMRI sessions each composed of 10 consecutive runs together with different preparatory and field inhomogeneity mapping scans (about 1h each). The last session was used to obtain multiple structural images (about 45 min in total). Participants were trained on the behavioral task outside the scanner.

Stimuli were presented at a viewing distance of 225 cm, on a 32-inch LCD screen (BOLDscreen, Cambridge Research Systems, Rochester, UK) situated at the end of the bore (17.8 dva horizontally by 10 dva vertically) and viewed through a mirror. The screen had a spatial resolution of 1920 by 1080 pixels and a refresh rate of 120 Hz. Button responses were collected using an MRI compatible button box (Current Designs, Philadelphia, PA, USA). The experimental software controlling the display and the response collection as well as eye tracking was implemented in Matlab (The MathWorks, Natick, MA, USA) using the Psychophysics Toolbox[61,62].

Participants were instructed to continuously fixate a white bull's-eye on a black background. The bull's-eye was composed of a central white dot of 0.04 dva radius surrounded by a white annulus of 0.4 dva radius and a line width of 0.04 dva. They were instructed to attend visual noise contained either within this central bull's-eye (*attend-fix* condition, 1st, 3rd, 5th, 7th and 9th run) or within a moving bar (*attend-bar* condition, 2nd, 4th, 6th, 8th and 10th run). Each functional session started with 4 runs in which the fixation bull's-eye was displayed at the screen center together with the moving bar traversing the entire screen (*full-screen* condition, 1st, 2nd, 3rd and 4th run). In the next 6 runs, the moving bar stimulus was displayed within a 4 dva radius aperture (0.04 dva width cosine edge between the visual noise and the background) surrounding the fixation bull's-eye. The bull's-eye was displayed either 4 dva to the left of the screen center (*gaze left* condition, 5th and 6th run), 4 dva to the right of the screen center (*gaze right* condition. 7th and 8th run) or at the screen center (*gaze center* condition, 9th and 10th run). *Full screen* runs lasted 195 seconds (150 TRs). They were composed of 9 interleaved periods with and without the presentation of visual noise. In periods without visual noise, the bull's-eye was shown alone for 13 seconds (10 TRs). In periods with the visual noise, the bar aperture movement direction was sequentially 180° (left), 270° (down), 0° (right) and 90° (up). The bar aperture could either be horizontally or vertically oriented, in order to be perpendicular to its movement direction. Its center moved in the bar direction on every TR by discrete steps of 0.56 dva, such that 18 vertical and 32 horizontal steps were necessary to traverse the entire screen. *Gaze left*, *gaze right* and *gaze center* runs lasted 158.6 seconds (122 TRs). They were composed of the same nine interleaved periods with and without the presentation of visual noise. Contrary to the *full screen* runs, the bar aperture movement direction was sequentially 180° (left), 0° (right), 180° (left) and 0°

(right) and the bar was always vertically oriented. Its center moved in the bar direction on every TR by 18 discrete steps of 0.22 dva to traverse the circular aperture centered on the bull's-eye. Visual noise contained within the bar aperture (1 dva width, with 0.04 dva width cosine lateral edges) and the bull's-eye was composed of distinct randomly generated pink noise (1/f) grayscale textures[63] (with individual pixel of 0.04 dva width). To probe visual attention, we filtered the orientation contained within the textures to generate clockwise and counterclockwise signal textures. We defined 15 different difficulty levels by either keeping randomly generated noise or by filtering contained orientation by a von Misses distribution with standard deviation values between 10^{-1} (large dispersion) to $10^{1.5}$ (narrow dispersion) centered around +45° or -45° relative to the vertical axis. Each bar presentations started with 400 ms of streams of unfiltered noise textures presented at 10 Hz in both the bull's-eye and the bar aperture. This period was followed by 600 ms of clockwise or counterclockwise streams of oriented filtered noise, later followed by 300 ms of unfiltered noise streams. The period with oriented filtered noise streams was highlighted to participants with the bull's-eye central dot displayed in black. The orientation of the filtered noise was selected randomly and independently every TR for both the bull's-eye and the bar aperture. Participants reported the orientation of filtered noise streams presented within the bar aperture (*attend-bar* condition) or the bull's-eye (*attend-fix* condition) with left (-45° or counter-clockwise) or right thumb button presses (45° or clockwise). The difficulty of the task was titrated by a staircase procedure following a 3 down 1 up rule adjusting for the attended stream, the orientation dispersion around ±45°. Staircases started at an intermediate difficulty value (level 10) on every run. Participants had until the end of the TR to press a button if no response was registered the corresponding staircase wasn't modified.

Anatomical data preprocessing

T1-weighted (T1w) images were corrected for intensity non-uniformity[64]. The T1w-reference was then skull-stripped. Brain tissue segmentation of cerebrospinal fluid (CSF), white-matter (WM) and gray-matter (GM) was performed on the brain-extracted T1w[65]. A T1w-reference map was next computed after registration of 4 T1w[66]. Brain surfaces were reconstructed using freesurfer[67] and the brain mask estimated previously was next refined[68], with the aid of the additional T2w acquisition. Finally, the surface reconstruction was manually edited to correct for pial segmentation errors near the boundary of the occipital lobe and the cerebellum.

Functional data preprocessing

For each of the 20 functional runs per participant (across all tasks and sessions), the following preprocessing was performed. First, a reference volume and its skull-stripped version were generated using a custom methodology of fMRIPrep[69]. Head-motion parameters with respect to the BOLD reference (transformation matrices, and six corresponding rotation and translation parameters) are estimated before any spatiotemporal filtering[70]. A fieldmap was estimated based on two echo-planar imaging (EPI) references with opposing phase-encoding directions[71]. Based on the estimated susceptibility distortion, a corrected EPI (echo-planar imaging) reference was calculated for a more accurate co-registration with the anatomical reference. The BOLD reference was then co-registered to the T1w FreeSurfer[72]. Co-registration was configured with twelve degrees of freedom to account for distortions remaining in the BOLD reference. The BOLD timeseries were resampled onto their original, native space by applying a single, composite transform to correct for head-motion and susceptibility distortions. Low frequency drift up to 0.01 Hz of the functional time series was removed using cosine drift regressors obtained from fMRIPrep. Functional signal units were next converted to z-score.

Regions of interest definition and pRF parameters

We first averaged the timeseries of the 8 *full screen* runs, irrespective of whether participants attended to the fixation bull's-eye or to the bar stimulus. We analyzed this *fiducial* averaged time series using an isotropic Gaussian pRF model[15]. The model included a visual design matrix (converting the visual stimulus

in an on-off contrast map for each TR), the position (x, y), the size (standard deviation of the Gaussian), as well a signal amplitude and signal baseline as parameters. The time series were fitted in two parts. The first part was a coarse spatial grid search of 40 linear steps in the 3 spatial model parameters: position (x, y), and size. A linear regression between the predicted and measured time series signal was used to determine the baseline and amplitude parameters. The best-fitting parameters of the first step were next used as the starting point of an optimization phase to produce finely tuned estimates. The visual stimulus was down sampled by a factor 8 for the first of these fitting stages. The grid search position and size parameters were distributed linearly within 20 dva from the center of the screen. In the fine search stage, we used a gradient descent algorithm starting from the obtained grid search parameters, leaving the parameter ranges essentially unconstrained. PRF polar angle maps were derived with the best explained pRF position parameters. The polar angle was drawn using *Pycortex*[73] on an inflated and flattened cortical visualization of individual participant anatomy. The explained variance of the model set as the coefficient of determination (R^2) was used to determine color transparency. From this analysis we manually defined for each participant 12 cortical visual regions of interests following pRF angle and eccentricity progression on the cortex as well as anatomical references. These regions include V1, V2 and V3, V3AB which unites V3A and V3B subregions, Lateral Occipital area (LO) which unites LO1 and LO2 subregions, Ventral Occipital (VO) including selective voxels of the ventral path, hMT+ which unites both MT and MST subregions, the inferior and superior part of the Intra Parietal Sulcus areas (iIPS and sIPS) and the inferior, superior and medial parts of the Pre Cenral Sulcus areas (iPCS, sPCS and mPCS). For each ROI, we defined the best-fitting voxels parameters as the 250 highest R^2 per ROI. We evaluated the effect of the task on the explained variance of the pRFs by taking the task-related time series independently.

Out-of-sample predictions

We first evaluated the explained variance of retinotopic or spatiotopic pRF models by applying the parameters obtained in the *full screen* conditons to the *gaze* conditions time series. To do so, we predicted out-of-set timeseries of the gaze conditions visual designs knowing the pRF parameters of the attention task-specific *full screen* condition to which we either subtracted ($pRFx_{gaze\ left} = pRFx_{full\ screen} - 4$) or added ($pRFx_{gaze\ right} = pRFx_{full\ screen} + 4$) the gaze direction change to the *pRFx* parameter. Signal amplitude (beta) and signal baseline parameters were also adjusted to fit with the new timeseries. Change in explained variance between condition was computed by subtracting the averaged R^2 observed in the *gaze left* and *gaze right* condition from the R^2 observed in the *gaze center* condition.

Fitting predictions

We refine our analysis by determining anew the model parameters in the gaze conditions. To do so, we kept the *pRFy* and *pRFsize* parameters obtained from the *full screen* runs, while fitting anew the *pRFx* parameter as well as amplitude and the baseline. To avoid any bias toward the retinotopic or the spatiotopic model, we started the coarse fitting procedure with *x* coordinate spatial grids centered either on the gaze or on the screen coordinates. The best model (highest R^2) was next used in the optimization phase to produce finely tuned parameters.

Bayesian decoding

We developed a novel method to probabilistically decode the position of our moving bar stimulus from the multivariate fMRI data, within a Bayesian framework. The method is based on the standard pRF model fitted on an independent training dataset from the same participant. Provided with a multivariate fMRI timeseries $Y = y_{1..n,1..t}$ with n voxels and t time points, the method yields a posterior distribution $p(x_{1..t}, h_{1..t} | Y)$ over possible stimulus positions x and heights h for every frame in the time series where a stimulus was presented. The method allows to probe what bar position is represented on the level of a given ROI, on a TR-to-TR basis.

By jointly sampling across all time points of the data concurrently, we took into account the hemodynamic delay and hemodynamic temporal smoothing in the estimation procedure. This is made computationally feasible by a state-of-the-art computational graph library developed for deep neural network training (Tensorflow), massively parallel graphics processing units for computation (GPUs), as well as Hamiltonian MCMC method[74], which exploits the exact gradient functions that the "*autodiff*" functionality that Tensorflow provide.

To obtain a posterior distribution over bar positions, given fMRI data, we first needed a likelihood function that describes the probability of the data given a stimulus time series S. Let's assume S a time series of 2D stimulus images. The likelihood function is the probability density function of a multivariate t distribution over the residuals of the pRF model with a covariance matrix Σ of a multivariate t-distribution with df degrees-of-freedom. Hence, $Y = pRF(S;\ \theta_{1..n}) + \epsilon$ where $\epsilon \sim t(0, \Sigma, df)$ and thus $p(Y|x_{1..t}, h_{1..t}; \theta_{1..n}, \Sigma, df) = t(Y - prf(S; \theta_{1..n});\ \Sigma, df)$ where pRF is the output of a standard pRF model for the image time series S, as described in the previous section, with voxelwise position, dispersion, amplitude, and baseline parameters $\theta_{1..n}$ estimated using standard pRF fitting methods on an independent training dataset.

The pRF function includes a convolution step where "neural" time series are convolved with a canonical hemodynamic response function. This means that the pixel intensities on timepoint t influence the residuals and thereby likelihoods of multiple frames of neural activity data (roughly between timepoint t and 20 seconds later). This also means that different dimensions of the likelihood function that are close together in time are correlated, necessitating more advanced samplers than traditional Gibbs sampling[75,76].

To estimate the noise covariance matrix Σ, we couldn't use the sample covariance of the residuals of the training set, because these estimates would be highly unstable in our data regime of sparse data (a few hundred time points) and a large number of dimensions[77]. Therefore, we estimated a regularized covariance matrix $\hat{\Sigma}$, using a method developed for decoding Gabor orientations from fMRI signals in early visual areas[16]. Specifically, the covariance matrix estimate $\hat{\Sigma}$ is a weighted sum of a diagonal covariance matrix $I \circ \tau\tau^T$, a perfectly correlated covariance matrix $\tau\tau^T$, and a matrix WW^T, where W is a $n \times m$ matrix with n the number of voxels and m the total number of pixels in a single stimulus image. Each element of the matrix W describes the linear weight of its respective pixel to the activation of its respective voxel. More specifically, this value is the probability density of the x and y coordinates for the multivariate Gaussian described by the pRF parameters θ for that voxel, multiplied by its estimated amplitude.

Thus, we assume that the covariance of the residuals of two voxels that have particularly similar pRF should generally be higher than that of those voxels of which the pRF do not overlap[16–18]. The complete formula for the estimated residual covariance matrix $\hat{\Sigma}$ is: $\hat{\Sigma} = \rho I \circ \tau\tau^T + (1 - \rho)\tau\tau^T + \sigma^2 WW^T$ where the vector $\tau > 0$, scalar $0 \leq \rho < 1$, and scalar $\sigma^2 \geq 0$ are estimated using maximum likelihood estimation on the residuals $Y^{training} - pRF(S^{training};\ \theta_{1..n})$ of the training data, using gradient descent optimization. However, the dimensionality of the stimulus time series S was so high (above 100,000) that it was infeasible to sample its posterior distribution. Moreover, its dimensions are not semantically meaningful. Therefore, we opted to drastically reduce the dimensionality of S using a two-parameter stimulus model $s(x, h)$ that returns a two-dimensional pixel image with a vertically centered bar of a fixed width, centered on the x coordinate and a height of h. We chose this stimulus model because both the x position and height of the bar varied over time in the gaze conditions. Note that, in the stimulus function, the pixel intensity rapidly but smoothly falls off as a sigmoidal function of distance to the border of the bar stimulus. Such a smooth functional form was necessary to keep the likelihood function differentiable and thereby Hammoltonian MCMC feasible. This way, the number of parameters of the likelihood function was heavily reduced to 2 times the number of timepoints: $p(Y|\ x_{1..t}, h_{1..t};\ \theta) = t(Y - pRF(s(x_{1..t}, h_{1..t});\ \theta_{1..n});\ \Sigma, df)$. We reduced this number a bit further by not estimating stimulus

properties for frames where there was no stimulus bar on the screen such that the model assumed these frames to be an empty screen with a fixation bull's-eye.

We used uniform priors on the estimated x coordinates, restricted between the leftmost and rightmost coordinates on the screen as well as uniform priors on the height of the stimulus bar between 0 and the height of the stimulus screen. This was achieved using bijective sigmoidal transformation functions. The entire procedure was implemented in TensorFlow 2 and packaged as a freely available Python package called Braincoder (https://github.com/Gilles86/braincoder).

As a first step, a 2D grid search (position by height) was performed for every time point separately, optimizing the likelihood function with respect to single frame x and h parameters, neglecting the covariance structure of the likelihood function. After this grid search, a maximum a posteriori (MAP) estimate for the entire time series $argmax\ p(\ x_{1..t}, h_{1..t}|Y)$ was estimated using gradient descent, starting from the values found in the grid search. Finally, this MAP estimate was used as a starting point for the NUTS MCMC sampler, a self-tuning Hamiltonian MCMC sampler[76], to obtain samples from the posterior $p(\ x_{1..t}, h_{1..t}|Y)$. We used 4 independent chains, with 250 steps and 500 samples per chain. After some experimenting, we settled on an acceptance probability of 0.3 to more effectively sample our highly complex 144-dimensional posterior distribution.

Reference frame index

We devised a reference frame index (RFI), based on earlier work on the topic[11,13]. This index contrasts the ability of a spatiotopic versus a retinotopic model to explain the observed data. Specifically, it expresses the difference in explained variance between the retinotopic and the spatiotopic model as a fraction of the sum of both explained variances. Hence, the index ranges between -1 (completely and exclusively consistent with spatiotiotopic reference frame) and 1 (completely and exclusively consistent with the retinotopic reference frame):

$$\mathrm{RFI} = \frac{\mathrm{EV}_{\mathrm{retinotopic}} - \mathrm{EV}_{\mathrm{spatiotopic}}}{\mathrm{EV}_{\mathrm{retinotopic}} + \mathrm{EV}_{\mathrm{spatiotopic}}}$$

Where EV is the reduction in variance from the raw data versus the residuals of the model fit $\mathrm{EV} = \mathrm{Var}\left(\mathrm{Y} - \widehat{\mathrm{Y}}\right) - \mathrm{Var}(\mathrm{Y})$. Note that for the out-of-sample predictions (Figure 3) of individual PRF time series, the variance is defined on real and predicted BOLD timeseries of individual voxels. For the decoding analysis (Figure 4) the variance is defined on the actual and the decoded spatial positions of the bar stimulus.

Statistics

For statistical comparisons we used SciPy[78] paired permutation test with 10,000 permutation bootstrapped iterations used to approximate the null distribution[79]. This procedure allows us to resample our data to create a distribution with randomly rearranged labels of the conditions to compare for each participant. We determined statistical significance by deriving two-tailed (see Results) *p* values for the comparison of the distributions of the compared conditions.

Data and code availability

We make available online our imaging dataset, including all derivatives and individual participant and group figures (openneuro.org/datasets/ds004091). Brain models with data analysis visualization are made available online (invibe.nohost.me/gazeprf) together with the experimental and data analyses codes (github.com/mszinte/gaze_prf).

Acknowledgments

We are grateful to the members of the Knapen and Dumoulin laboratories in Amsterdam for helpful comments and discussions and to Alice and Clémence Szinte for their support. Centre de Calcul Intensif

d'Aix-Marseille is acknowledged for granting access to its high performance computing resources. This research was supported by a Marie Skłodowska-Curie Action Individual Fellowship to M.S. (704537) and an NWO-CAS (012.200.012) and ABMP (2015-7) grants to T.K.

Author contributions

Conceptualization, M.S., and T.K.; Methodology, M.S., G.H., M.A., and T.K.; Software, M.S., G.H., M.A., and T.K.; Validation, M.S., G.H., M.A., and T.K.; Formal Analysis, M.S., G.H., M.A., and T.K.; Investigation, M.S., I.V., and T.K.; Resources, T.K.; Data Curation, M.S.; Writing – Original Draft, M.S., G.H., and T.K.; Writing – Review & Editing, M.S., G.H., M.A., I.V., S.D., and T.K.; Visualization, M.S., G.H. and T.K.; Supervision, S.D., T.K.; Project Administration, T.K.; Funding Acquisition, M.S. and T.K.

References

1. Baylor, D. A., Lamb, T. D. & Yau, K. W. Responses of retinal rods to single photons. *J Physiology* **288**, 613–634 (1979).
2. Sereno, M. I. *et al.* Borders of multiple visual areas in humans revealed by functional magnetic resonance imaging. *Science* **268**, 889–893 (1995).
3. Wandell, B. A., Dumoulin, S. O. & Brewer, A. A. Visual field maps in human cortex. *Neuron* **56**, 366–383 (2007).
4. Zeki, S. M. Functional organization of a visual area in the posterior bank of the superior temporal sulcus of the rhesus monkey. *J Physiology* **236**, 549–573 (1974).
5. Essen, D. C. V., Maunsell, J. H. R. & Bixby, J. L. The middle temporal visual area in the macaque: Myeloarchitecture, connections, functional properties and topographic organization. *The Journal of comparative neurology* **199**, 293–326 (1981).
6. Snyder, L. H., Batista, A. P. & Andersen, R. A. Coding of intention in the posterior parietal cortex. *Nature* **386**, 167–170 (1997).
7. Fabius, J. H., Moravkova, K. & Fracasso, A. Topographic organization of eye-position dependent gain fields in human visual cortex. *Nat Commun* **13**, 7925 (2022).
8. Andersen, R. A. & Mountcastle, V. B. The influence of the angle of gaze upon the excitability of the light-sensitive neurons of the posterior parietal cortex. *The Journal of Neuroscience* **3**, 532–548 (1983).
9. Andersen, R. A., Snyder, L. H., Bradley, D. C. & Xing, J. Multimodal representation of space in the posterior parietal cortex and its use in planning movements. *Annual Review of Neuroscience* **20**, 303–330 (1997).
10. Andersen, R. A., Essick, G. K. & Siegel, R. M. Encoding of spatial location by posterior parietal neurons. *Science* **230**, 456–458 (1985).
11. Crespi, S. *et al.* Spatiotopic Coding of BOLD Signal in Human Visual Cortex Depends on Spatial Attention. *PLoS ONE* **6**, (2011).
12. d'Avossa, G. *et al.* Spatiotopic selectivity of BOLD responses to visual motion in human area MT. **10**, 249–255 (2007).
13. Gardner, J. L., Merriam, E. P., Movshon, J. A. & Heeger, D. J. Maps of Visual Space in Human Occipital Cortex Are Retinotopic, Not Spatiotopic. *The Journal of Neuroscience* **28**, 3988–3999 (2008).
14. Golomb, J. D. & Kanwisher, N. Higher Level Visual Cortex Represents Retinotopic, Not Spatiotopic, Object Location. *Cereb Cortex* **22**, 2794–2810 (2012).
15. Dumoulin, S. O. & Wandell, B. A. Population receptive field estimates in human visual cortex. *NeuroImage* **39**, 647–660 (2008).
16. Bergen, R. S. van, Ma, W. J., Pratte, M. S. & Jehee, J. F. M. Sensory uncertainty decoded from visual cortex predicts behavior. *Nature neuroscience* **18**, 1728–1730 (2015).
17. Bergen, R. S. van & Jehee, J. F. M. Probabilistic Representation in Human Visual Cortex Reflects Uncertainty in Serial Decisions. *J Neurosci* **39**, 8164–8176 (2019).

18. Bergen, R. S. van & Jehee, J. F. M. Modeling correlated noise is necessary to decode uncertainty. *Neuroimage* **180**, 78–87 (2018).
19. Anton-Erxleben, K. & Carrasco, M. Attentional enhancement of spatial resolution: linking behavioural and neurophysiological evidence. *Nature reviews. Neuroscience* **14**, 188–200 (2013).
20. Carrasco, M. Visual attention: The past 25 years. *Vision Research* **51**, 1484–1525 (2011).
21. Bressler, D. W. & Silver, M. A. Spatial attention improves reliability of fMRI retinotopic mapping signals in occipital and parietal cortex. *Neuroimage* **53**, 526–533 (2010).
22. Silver, M. A., Ress, D. & Heeger, D. J. Topographic Maps of Visual Spatial Attention in Human Parietal Cortex. *J Neurophysiol* **94**, 1358–1371 (2005).
23. Geurts, L. S., Cooke, J. R. H., Bergen, R. S. van & Jehee, J. F. M. Subjective confidence reflects representation of Bayesian probability in cortex. *Nat Hum Behav* **6**, 294–305 (2022).
24. Aqil, M., Knapen, T. & Dumoulin, S. O. Divisive normalization unifies disparate response signatures throughout the human visual hierarchy. *Proc National Acad Sci* **118**, e2108713118 (2021).
25. Klein, B. P., Harvey, B. M. & Dumoulin, S. O. Attraction of position preference by spatial attention throughout human visual cortex. *Neuron* **84**, 227–237 (2014).
26. Es, D. M. van, Theeuwes, J. & Knapen, T. Spatial sampling in human visual cortex is modulated by both spatial and feature-based attention. *eLife* **7**, 3771 (2018).
27. Sun, L. D. & Goldberg, M. E. Corollary Discharge and Oculomotor Proprioception: Cortical Mechanisms for Spatially Accurate Vision. *Annual Review of Vision Science* **2**, 61–84 (2016).
28. Neupane, S., Guitton, D. & Pack, C. C. Perisaccadic remapping: What? How? Why? *Rev Neuroscience* **31**, 505–520 (2020).
29. Andersen, R. A., Essick, G. K. & Siegel, R. M. Encoding of Spatial Location by Posterior Parietal Neurons. *Science* **230**, 456–458 (1985).
30. Durand, J.-B., Trotter, Y. & Celebrini, S. Privileged processing of the straight-ahead direction in primate area V1. *Neuron* **66**, 126–137 (2010).
31. Trotter, Y. & Celebrini, S. Gaze direction controls response gain in primary visual-cortex neurons. *Nature* **398**, 239–242 (1999).
32. Andersen, R. & Mountcastle, V. The influence of the angle of gaze upon the excitability of the light-sensitive neurons of the posterior parietal cortex. *J Neurosci* **3**, 532–548 (1983).
33. Morris, A. P. & Krekelberg, B. A Stable Visual World in Primate Primary Visual Cortex. *Curr Biol* **29**, 1471-1480.e6 (2019).
34. Arthurs, O. J. & Boniface, S. How well do we understand the neural origins of the fMRI BOLD signal? *Trends Neurosci* **25**, 27–31 (2002).
35. Sirotin, Y. B. & Das, A. Anticipatory haemodynamic signals in sensory cortex not predicted by local neuronal activity. *Nature* **457**, 475–479 (2009).
36. Zhao, Z., Ahissar, E., Victor, J. D. & Rucci, M. Inferring visual space from ultra-fine extra-retinal knowledge of gaze position. *Nat Commun* **14**, 269 (2023).
37. Sperry, R. W. Neural basis of the spontaneous optokinetic response produced by visual inversion. *Journal of comparative and physiological psychology* **43**, 482–489 (1950).
38. Sommer, M. A. & Wurtz, R. H. Influence of the thalamus on spatial visual processing in frontal cortex. *Nature* **444**, 374–377 (2006).
39. Duhamel, J. R., Colby, C. L. & Goldberg, M. E. The Updating of the Representation of Visual Space in Parietal Cortex by Intended Eye-Movements. *Science* **255**, 90–92 (1992).
40. Cavanagh, P., Hunt, A. R., Afraz, A. & Rolfs, M. Visual stability based on remapping of attention pointers. *Trends in Cognitive Sciences* **14**, 147–153 (2010).
41. Rolfs, M. & Szinte, M. Remapping Attention Pointers: Linking Physiology and Behavior. *Trends in Cognitive Sciences* **20**, 399–401 (2016).
42. Wurtz, R. H. Neuronal mechanisms of visual stability. *Vision Research* **48**, 2070–2089 (2008).

43. Merriam, E. P., Genovese, C. R. & Colby, C. L. Spatial Updating in Human Parietal Cortex. *Neuron* **39**, 361–373 (2003).
44. Merriam, E. P., Genovese, C. R. & Colby, C. L. Remapping in Human Visual Cortex. *Journal of Neurophysiology* **97**, 1738–1755 (2007).
45. Knapen, T., Swisher, J. D., Tong, F. & Cavanagh, P. Oculomotor Remapping of Visual Information to Foveal Retinotopic Cortex. *Frontiers in Systems Neuroscience* **10**, 54 (2016).
46. Rolfs, M., Jonikaitis, D., Deubel, H. & Cavanagh, P. Predictive remapping of attention across eye movements. *Nature neuroscience* **14**, 252–256 (2011).
47. Szinte, M., Jonikaitis, D., Rangelov, D. & Deubel, H. Pre-saccadic remapping relies on dynamics of spatial attention. *eLife* **7**, e37598 (2018).
48. Womelsdorf, T., Anton-Erxleben, K. & Treue, S. Receptive field shift and shrinkage in macaque middle temporal area through attentional gain modulation. *The Journal of Neuroscience* **28**, 8934–8944 (2008).
49. Campbell, M. G. *et al.* Principles governing the integration of landmark and self-motion cues in entorhinal cortical codes for navigation. *Nat Neurosci* **21**, 1096–1106 (2018).
50. Mallory, C. S. *et al.* Mouse entorhinal cortex encodes a diverse repertoire of self-motion signals. *Nat Commun* **12**, 671 (2021).
51. Arnoldussen, D. M., Goossens, J. & Berg, A. V. van den. Adjacent visual representations of self-motion in different reference frames. *Proc National Acad Sci* **108**, 11668–11673 (2011).
52. Lescroart, M. D. & Gallant, J. L. Human Scene-Selective Areas Represent 3D Configurations of Surfaces. *Neuron* **101**, 178-192.e7 (2019).
53. Bonner, M. F. & Epstein, R. A. Coding of navigational affordances in the human visual system. *Proc National Acad Sci* **114**, 4793–4798 (2017).
54. Epstein, R. A. & Baker, C. I. Scene Perception in the Human Brain. *Annu Rev Vis Sc* **5**, 1–25 (2019).
55. Purandare, C. S. *et al.* Moving bar of light evokes vectorial spatial selectivity in the immobile rat hippocampus. *Nature* **602**, 461–467 (2022).
56. Saleem, A. B., Diamanti, E. M., Fournier, J., Harris, K. D. & Carandini, M. Coherent encoding of subjective spatial position in visual cortex and hippocampus. *Nature* **562**, 124–127 (2018).
57. Diamanti, E. M. *et al.* Spatial modulation of visual responses arises in cortex with active navigation. *Elife* **10**, e63705 (2021).
58. Knapen, T. Topographic connectivity reveals task-dependent retinotopic processing throughout the human brain. *Proc National Acad Sci* **118**, e2017032118 (2020).
59. Nau, M., Schröder, T. N., Bellmund, J. L. S. & Doeller, C. F. Hexadirectional coding of visual space in human entorhinal cortex. *Nat Neurosci* **21**, 188–190 (2018).
60. Oliveira, Í. A. F., Roos, T., Dumoulin, S. O., Siero, J. C. W. & Zwaag, W. van der. Can 7T MPRAGE match MP2RAGE for gray-white matter contrast? *Neuroimage* **240**, 118384 (2021).
61. Pelli, D. G. The VideoToolbox software for visual psychophysics: transforming numbers into movies. *Spatial Vision* **10**, 437–442 (1997).
62. Brainard, D. H. The Psychophysics Toolbox. *Spatial Vision* **10**, 433-436. (1997).
63. Hanning, N. M., Deubel, H. & Szinte, M. Sensitivity measures of visuospatial attention. *Journal of Vision* **19**, 17–17 (2019).
64. Tustison, N. J. *et al.* N4ITK: Improved N3 Bias Correction. *Ieee T Med Imaging* **29**, 1310–1320 (2010).
65. Zhang, Y., Brady, M. & Smith, S. Segmentation of Brain MR Images Through a Hidden Markov Random Field Model and the Expectation-Maximization Algorithm. *Ieee T Med Imaging* **20**, 45 (2001).
66. Reuter, M., Rosas, H. D. & Fischl, B. Highly accurate inverse consistent registration: A robust approach. *Neuroimage* **53**, 1181–1196 (2010).
67. Dale, A. M., Fischl, B. & Sereno, M. I. Cortical Surface-Based Analysis: I. Segmentation and Surface Reconstruction. *NeuroImage* **9**, 179–194 (1999).
68. Klein, A. *et al.* Mindboggling morphometry of human brains. *Plos Comput Biol* **13**, e1005350 (2017).

69. Esteban, O. *et al.* fMRIPrep: a robust preprocessing pipeline for functional MRI. *Nature Methods* **16**, 111–116 (2019).
70. Jenkinson, M., Bannister, P., Brady, M. & Smith, S. Improved Optimization for the Robust and Accurate Linear Registration and Motion Correction of Brain Images. *Neuroimage* **17**, 825–841 (2002).
71. Cox, R. W. & Hyde, J. S. Software tools for analysis and visualization of fMRI data. *Nmr Biomed* **10**, 171–178 (1997).
72. Greve, D. N. & Fischl, B. Accurate and robust brain image alignment using boundary-based registration. *Neuroimage* **48**, 63–72 (2009).
73. Gao, J. S., Huth, A. G., Lescroart, M. D. & Gallant, J. L. Pycortex: an interactive surface visualizer for fMRI. *Frontiers in neuroinformatics* **9**, 162 (2015).
74. Betancourt, M. A Conceptual Introduction to Hamiltonian Monte Carlo. *Arxiv* (2017).
75. Turner, B. M., Sederberg, P. B., Brown, S. D. & Steyvers, M. A Method for Efficiently Sampling From Distributions With Correlated Dimensions. *Psychol Methods* **18**, 368–384 (2013).
76. Hoffman, M. D. & Gelman, A. The No-U-Turn Sampler: Adaptively Setting Path Lengths in Hamiltonian Monte Carlo. *Journal of Machine Learning Research* **15**, 1593–1623 (2014).
77. Ledoit, O. & Wolf, M. Improved estimation of the covariance matrix of stock returns with an application to portfolio selection. *J Empir Financ* **10**, 603–621 (2003).
78. Virtanen, P. *et al.* SciPy 1.0: Fundamental Algorithms for Scientific Computing in Python. *Nature Methods* **17**, 261–272 (2020).
79. Ernst, M. D. Permutation Methods: A Basis for Exact Inference. *Stat Sci* **19**, (2004).

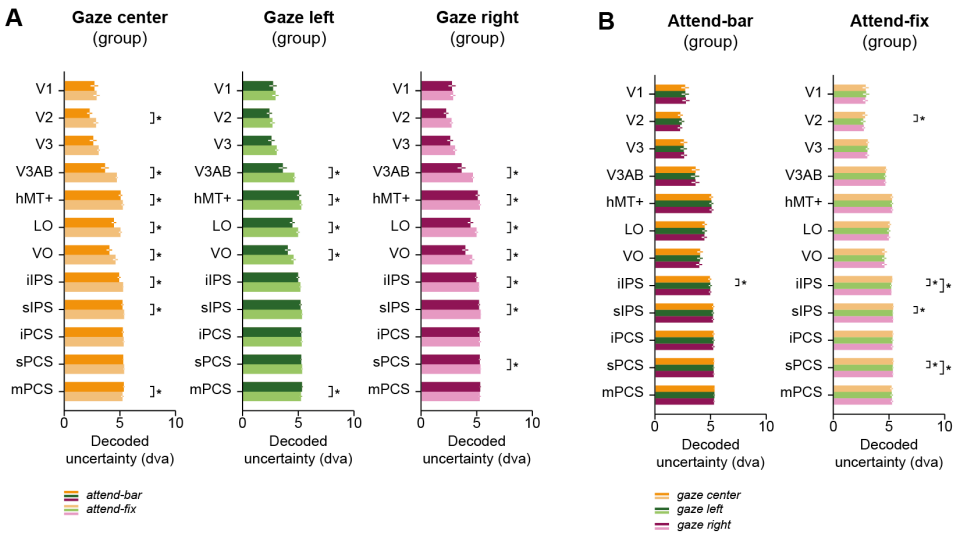

Figure S1. Decoding uncertainty. A. Average decoded uncertainty across ROIs and participants for the gaze center (left column), gaze left (middle column) and gaze right (right column) conditions. Black asterisks indicate a significant difference between the *attend-bar* and *attend-fix* conditions (two-sided $p < 0.05$). **B.** Same results for the attend-bar (left column) and attend-fix (right column) conditions. Black asterisks indicate a significant difference between the *gaze center*, *gaze left* and *gaze right* conditions (two-sided $p < 0.05$).

1